This article has been accepted for publication in IEEE Journal of the Electron Devices Society. This is the author's version which has not been fully edited and content may change prior to final publication. Citation information: DOI 10.1109/JEDS.2026.3653490

Photo-modulated reflectance for monitoring of the annealing of implanted Si samples

D. Ullrich[1,2], J. Szivós[1], B. Dénes[1], Z. Deli[1], G. Fekete[1], Z. Bozóki[1], S. Lenk[2], Z. Zolnai[1], G. Nádudvari[1], L. Balogh[1]

[1]Semilab Semiconductor Physics Laboratory Ltd, Prielle Kornélia u. 2. H-1117 Budapest, Hungary

[2]Department of Atomic Physics, Institute of Physics, Budapest University of Technology and Economics, Műegyetem rkp 3., H-1111 Budapest, Hungary

Abstract- Photo-modulated reflectance (PMR) is a sensitive optical technique applied for monitoring implantation-induced damage in Si wafers. In this work, we demonstrate that PMR is suitable for the characterization of Si wafers annealed by both melting and non-melting laser annealing methods. The PMR signal shows a linear correlation with normalized laser energy density, with $R^2 = 0.944$ (melting) and $R^2 = 0.957$ (non-melting), which is consistent with four-point probe sheet resistance and thermal annealing relation. These results confirm that PMR provides a fast, non-destructive and non-contact metrology for evaluating annealed wafers, offering potential for precise inline process control.

Index Terms— as-implanted Si wafer, four-point probe, inline metrology, melting and non-melting laser annealing, photo-modulated reflectance.

I. INTRODUCTION

Photo-modulated reflectance (PMR) [1][2][3] is an optical technique that measures variations in the optical reflectivity of a material induced by modulated light excitation. PMR is a powerful method for analyzing the effects of ion implantation in silicon (Si) wafers, for as-implanted state before thermal annealing. PMR is highly sensitive to implantation-induced crystal damage, which is primarily influenced by implantation parameters such as ion species, dose, energy, tilt angle, and ion beam current [4][5].

Ion implantation introduces defects [6] that reduce the electrical conductivity of the exposed region of the wafer. To restore and precisely control conductivity, thermal annealing is used to repair the crystal structure and activate the implanted dopants [6]. Since the annealing parameters control the degree of damage recovery, they are also in close connection with the PMR response.

In this work, we demonstrate that PMR is not only effective for characterizing as-implanted Si wafers, but also for samples post-annealed by laser beam exposure. Here we compare Si samples treated by melting and non-melting laser annealing processes with different laser energy densities in different areas of the wafers. Both melting and non-melting laser annealing can repair implantation-induced damage in Si wafers [7][8][9]. Melting annealing can heat the surface above the melting point for rapid recrystallization, while non-melting keeps the temperature below the melting point or prevents the sample from full melting due to lack of latent heat required for full melting of the heated zone at the melting temperature.

Besides PMR analysis, complementary four-point probe (4pp) measurements were also carried out in all regions of the wafers. Our results confirm that the PMR signal remains sensitive to residual crystal damage after laser annealing and it correlates with the electrically activated carrier concentration reflected in the sheet resistance [12]. A stronger correlation is observed in the non-melted sample, while in the melted one the correlation was weaker, highlighting differences in damage recovery and activation behavior between the two laser annealing modes.

Furthermore, PMR enables high-resolution monitoring of the ion implantation process uniformity on the lateral scale. These capabilities offer comprehensive approach to process optimization, characterization and quality control with a non-destructive and non-contact technique in semiconductor industry.

II. MATERIAL AND METHODS

The principle of operation of the PMR technique is based on the illumination of the sample with two laser sources of different wavelengths: probe (980 nm) and pump (808 nm). The intensity of the pumping laser is modulated by a 2 kHz signal, thus generating excess charge carrier pulses and inducing localized heating periodically. These effects create a quasi-static change in the refractive index of the material. The probe laser, using lock-in technique [1][2][10][11], detects the relative reflectance change which is defined as the PMR signal value (i.e., $\Delta R/R \times 10^6$),

The photon energy of the pump laser surpasses the bandgap of the Si samples; thus, it generates hot carriers and heat which leads to change of optical properties. The approximate penetration depths of the pump and probe lasers are ~10 µm and ~100 µm, respectively, providing an optimal balance between excitation and detection depth while ensuring high signal-to-noise ratio without optical aberrations.

A single cycle of the PMR measurement was carried out at ~400 sites on both investigated wafers. The radius of the 2 overlapping pumping and probe laser spots is 1.5 µm at the wafer surface. Toshiba Electronic Devices and Storage Corporation (Japan) prepared two pieces of 12-inch Silicon wafers. The crystallographic orientation is [100], the thickness of the wafers is 775 µm, the resistivity is 8-12 Ωcm, and the impurity type is boron with a concentration of $1.1 - 1.66 \times 10^{15} cm^{-3}$. The wafers were implanted with

This article has been accepted for publication in IEEE Journal of the Electron Devices Society. This is the author's version which has not been fully edited and content may change prior to final publication. Citation information: DOI 10.1109/JEDS.2026.3653490

phosphorus ions at a dose of $5 \times 10^{13} ions/cm^2$ and energy of 300 keV.

The laser-annealing spot was rectangular with millimeter-scale dimensions. The nominal wafer edge-exclusion is 2 mm. Within the edge-exclusion zone, adjacent rectangles extend beyond each other; the nominal values were not precisely known by the sample manufacturer, as these parameters had not been previously measured or determined. Different regions of the wafer were treated with different laser power, and the schematic spatial distribution of the annealing laser energy is shown in Figure 1. We report normalized laser energy densities in Table 1.

Number of regions	Relative laser energy densities of melting case	Relative laser energy densities of non-melting case
1	0.600	0.886
2	0.650	0.900
3	0.700	0.914
4	0.750	0.929
5	0.800	0.943
6	0.850	0.957
7	0.900	0.971
8	0.950	0.986
9	1.000	1.000
10	0.000	0.000

Table 1.: Relative laser energy densities for melting and non-melting annealing cases.

In the melting annealing condition, a shorter-wavelength laser was used, causing stronger surface absorption and partial (or total) surface melting. In contrast, the non-melting condition employed a longer-wavelength laser, which penetrated deeper and heated the wafer below the melting temperature. Because of the difference in absorption depth, identical laser energy-density steps could not be applied, resulting in a larger intensity ratio between steps in the non-melting case.

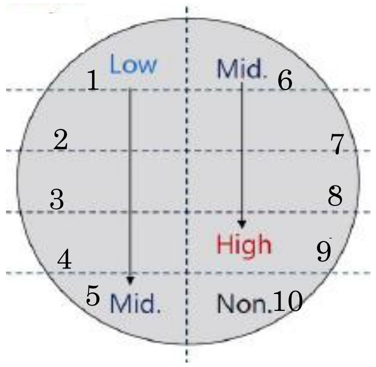

Figure 1.: Energy density distribution of the laser annealing in the 10 regions of the Si wafer. The 10th region was not annealed.

The 4pp measurements were performed on the same regions of the wafers, in 5 measurement points per region in 5 cycles, to determine the sheet resistance. It provided the average resistance over a millimeter-scale contact spacing. Based on the 4pp results, correlation between the PMR signal and the electrically activated carrier concentrations could be established. In the graphical representation of the results (Fig. 3 and Fig. 4), the PMR signals recorded from the non-annealed regions are excluded to enhance the visibility of small changes. Measurements were taken at the locations indicated in the figures by dots, and the results are presented using pseudo colors after surface fitting, on a scale ranging from blue (negative values) to red (positive values).

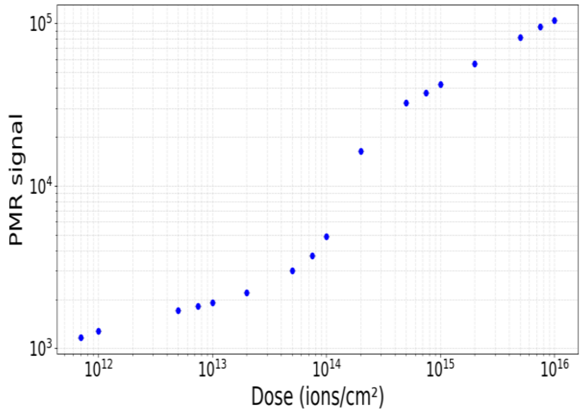

Figure 2.: PMR signal as a function of implantation P$^+$ dose., 50 keV, room temperature, non-channeling and non-annealed.

To benchmark PMR sensitivity versus implantation dose, we also measured a general "dose ladder" on implanted Si: P$^+$ ion, 50 keV, room temperature, no channeling; The crystal orientation is [100], thickness of the wafers is 725 µm, the resistivity is 15-25 Ωcm and the impurity type is boron. In Fig. 2, the PMR signal increases monotonically with dose over 5 orders of magnitude, even above the amorphization threshold.

III.RESULTS AND DISCUSSION

Our findings, depicted in Fig. 3. and 4. show the impact of the annealing conditions and their correlation with annealing induced crystal damage recovery. Note, the typical PMR

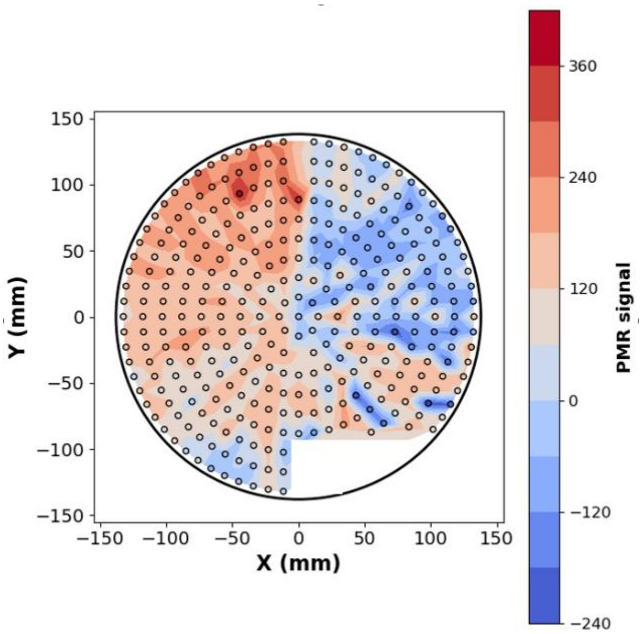

Figure 3.: PMR signal results of the melting laser annealed Si wafer. The open circles represent the locations of the PMR measurements.

This article has been accepted for publication in IEEE Journal of the Electron Devices Society. This is the author's version which has not been fully edited and content may change prior to final publication. Citation information: DOI 10.1109/JEDS.2026.3653490

signal value in the as-implanted zone is 4000 due to the high amount of damage left behind by the 300 keV P^+ ions during the implantation process.

Fig. 3 shows the PMR measurement results for melting laser annealing. These conditions produced less homogeneous PMR signals across different annealed regions compared to the non-melting laser annealing conditions in Fig. 4.

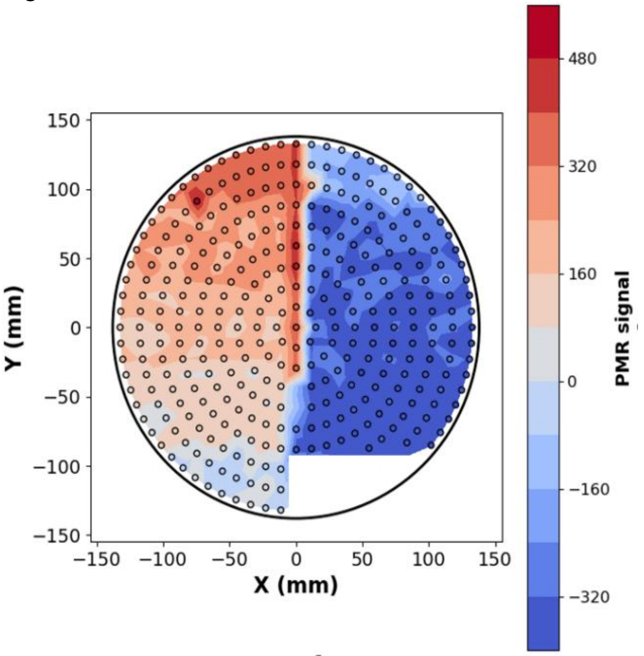

Figure 4.: PMR signal results of the non-melting laser annealed Si wafer. The open circles represent the locations of the PMR measurement

Also, the results show that as the laser energy density increases from the low level to high level, the PMR signals monotonously decrease for both melting and non-melting cases. Both results show that the PMR signal changes sign at a certain laser annealing energy density level. Since the PMR signal is proportional to the relative change of the reflection coefficient, this negative sign means that the reflection coefficient of the material decreases under the influence of the generating laser. This trend is characteristic of the (restored) crystalline Si.

This behavior can be explained by two opposing processes determining the PMR signal. The temperature increase, due to the heat induced by the generation laser, increases the reflection coefficient (thermo-optical effect), while the increased concentration of excited charge carriers decreases it (electro-optical effect). As annealing-induced damage recovery and recrystallization eliminates structural defects in the laser annealed region, the concentration and lifetime of the generated charge carriers change. In regions of effective damage recovery, the electro-optical effect may dominate the PMR signal. This relationship is expressed in Equation 1:

$$Signal_{PMR} \approx \left|\frac{4}{1-n^2}\right| \left[\delta \Delta T - \frac{|\beta| \Delta N}{m_e} - \frac{|\beta| \Delta P}{m_h}\right] \quad (1)$$

where, n is the refractive index, δ is thermo-optic coefficient and β is the electro-optic coefficient. ΔN and ΔP represent the excess electron and hole concentrations generated by the pump laser, and m_e and m_h are the effective masses of the electron and hole. ΔT is the temperature change [3]. This equation shows only the first order approximation of the signal. Consequently, in a less damaged region, with less structural defect centers for carrier recombination, the excess carrier concentration increases, while the temperature rises (partly due to recombination-induced energy transfer to the lattice through structural defects) decreases, resulting in a more negative PMR signal value.

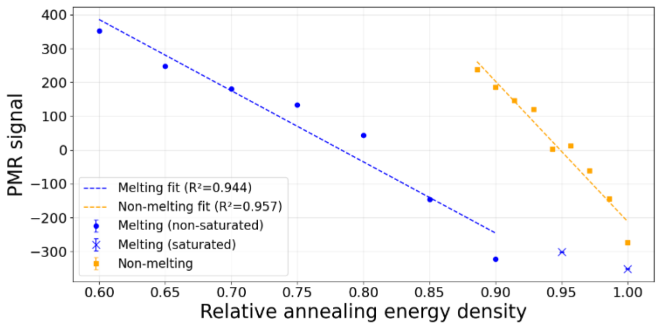

Figure 5.: Average PMR signal as a function of relative laser energy density with linear fits. Blue dots: melting annealed wafer. Orange squares: non-melting annealed wafer. The error bars represent the weighted deviations of the measurements, although they are insignificant compared to data symbols and thus hardly visible.

Figure 5. presents the average results of 5-point PMR measurements as a function of the laser energy densities. Above a certain annealing energy density, the crystal damage recovery saturates, leading to a final stable state. This saturation was observed in the melting case on the right side of the wafer in the last 2 regions. A linear relationship can be observed between the PMR signal and the laser annealing energy density, with R^2 values of 0.95 and 0.96 for the melting and non-melting conditions, respectively. For the melting case, the PMR signals were fitted from the 1st to the 7th region.

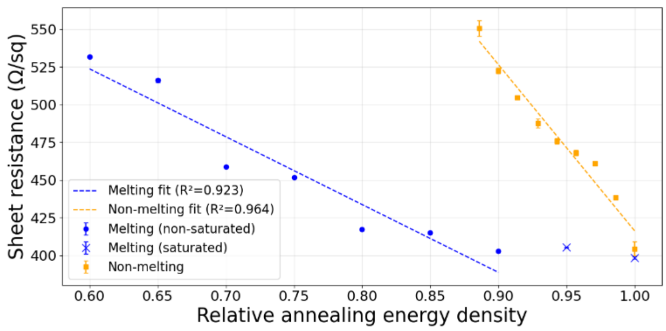

Figure 6.: Average sheet resistance as a function of relative laser energy density with linear fits. Blue dots: melting annealed wafer. Orange squares: non-melting annealed wafer. The error bars represent the weighted deviations of the measurements, although they are insignificant compared to data symbols and thus hardly visible.

This article has been accepted for publication in IEEE Journal of the Electron Devices Society. This is the author's version which has not been fully edited and content may change prior to final publication. Citation information: DOI 10.1109/JEDS.2026.3653490

A similar trend was confirmed by our 4pp measurements, see Fig. 6., which revealed that the sheet resistance decreased with energy density and reached a stable minimum in the last two melting sample regions. The R^2 values of the fit are 0.923 in melting and 0.964 in non-melting conditions.

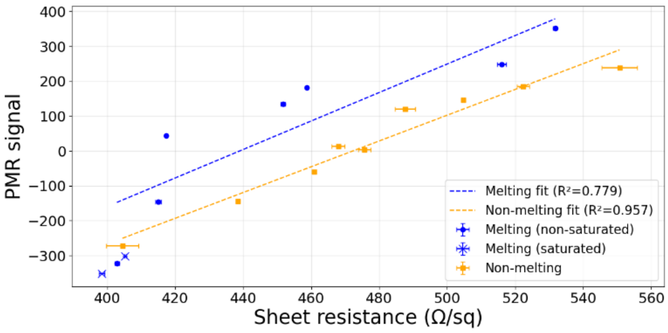

Figure 7.: Average PMR signal as a function of sheet resistance with linear fits. Blue dots: melting annealed wafer. Orange squares: non-melting annealed wafer. The error bars represent the weighted deviations of the measurements, although they are insignificant compared to data symbols and thus hardly visible.

This demonstrates that both the PMR signal and sheet resistance track the same physical processes: the activation of implanted dopant concentrations and the recovery of crystal lattice damage, which together determine the conductivity of the activated layer [15]. Although an analytical expression for PMR versus conductivity is not yet available, our experiments demonstrate that the PMR signal depends strongly on crystal damage, either implantation-induced or residual after annealing.

In the as-implanted state, the sheet resistance of Si increases with crystal damage compared to bare Si. Since the damage effect increases the number of defects, the resistance is not measurable by 4pp, whereas PMR remains sensitive. As annealing progresses the damage decreases, reducing both the resistance and the PMR signal. Once sufficient recrystallization and dopant activation occurs, the 4pp becomes sensitive again and measures a sheet resistance characteristic for the electrically activated layer. For the non-melting sample regime, the PMR signal-sheet resistance correlation was excellent ($R^2 = 0.957$), while for the melting regime, it was weaker ($R^2 = 0.779$), see Fig. 7. The slope and intercept for the melting case are $s_m = 4.08$ PMR unit /Ω/sq and $I_m = -1792.5$ PMR unit, while for the non-melting case they are $s_{nm} = 3.69$ PMR unit /Ω/sq and $I_{nm} = -1744.8$ PMR unit. Here, the PMR unit corresponds to the dimensionless quantity $\Delta R/R \times 10^6$. The different slopes reflect the distinct activation states (built-in impurity concentrations) and defect-recovery profiles for the two annealing conditions.

The PMR signal for the unimplanted, unannealed reference wafer was −889, representing the characteristic negative sign for single crystalline Si. Upon recrystallization, the PMR signal for the annealed samples also shows a negative sign.

However, it does not reach the value of the reference and, consequently, the sheet resistance of the activated shallow layer is also higher. The sheet resistance of the reference sample is based on the resistivity and thickness of the bulk: $R_s \sim 10$ Ωcm / 775 µm = 129 Ω/sq. Because of the thinner activated layer (few 100 nm range) [14] and the p-n depletion region, for the highest laser annealing energy densities in Fig. 6, the sheet resistance shows higher values at about 400 Ω/sq.

Interestingly, in the non-melting case the error bars are noticeably larger, reflecting higher local variability; nevertheless, the overall trend is more consistent. In contrast, the melting data show smaller scatters, yet the correlation is weaker. One possible explanation is that melting annealing creates a very shallow, highly doped surface layer with increased density of surface states. These defects enhance the surface recombination velocity, which strongly affects the optically generated carriers detected by PMR [13].

Additionally, examination was carried out in the edge-exclusion zone for both wafers. In this zone the PMR measurements could perfectly reveal the stair arrangement of the annealing treatments, see Fig, 8. and Fig. 9. The PMR mapping clearly demonstrates the extent of the overhangs of annealing laser spot. Confirming its capability to visualize even such small process-related geometrical variations. Based on the PMR data, the actual overhang dimensions were estimated to be 1.6 mm × 0.6 mm for the melting case, and 2.0 mm × 0.6 mm for the non-melting case. This observation points out the PMR metrology may serve as useful inline tool for verifying the annealing system alignment and for checking the programmed pattern accuracy. Furthermore, the effective edge-exclusion was found to be approximately 2.3 mm, based on the coordinates of the sharp corner and the wafer's circular geometry.

Note, PMR has a great advantage compared to the four-point probe resistance measurements as the latter have an edge-exclusion of approximately 5 mm and a resolution of a few millimeters. In contrast, the PMR laser spot radius is ~1.5 µm that allows a spatial resolution down to 10 µm that

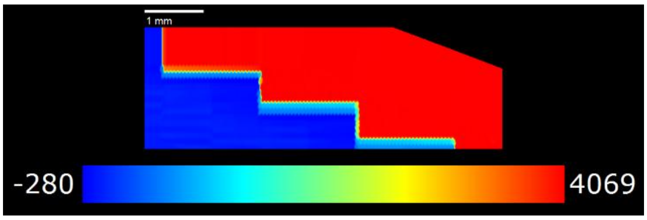

Figure 8.: PMR signal results in the edge zone in the 6th region of the-melting annealed wafer.
The scale bar is 1 mm

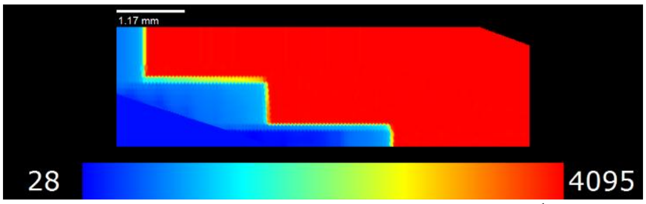

Figure 9.: PMR signal results in the edge zone in the 6th region of the non-melting annealed wafer.
The scale bar is 1.17 mm.

is much smaller than the annealing laser spots. The wafer edge-exclusion is <1 mm. This way, a high-resolution mapping of the result of annealing becomes possible.

IV. CONCLUSION

In this work, it was presented that PMR, as a non-contact, non-destructive process characterization tool can be applied for monitoring of melting and non-melting laser annealing effects in ion implanted Si with good sensitivity for the laser annealing energy density and with excellent lateral resolution, and small edge-exclusion.

In addition to mapping annealing assisted recovery of implantation-induced crystal damage, we established a direct correlation between PMR signals and four-point probe (4pp) sheet resistance measurements. A strong linear relationship was found in the non-melting laser annealing regime, confirming that PMR can reliably track changes related to electrically activated dopant concentration.

ACKNOWLEDGMENT

We would like to express our gratitude to Toshiba Electronic Devices and Storage Corporation (Japan) for enabling the publication of the results.

References

[1] F. Dortu, Low Frequency Modulated Optical Reflectance for the One-Dimensional Characterization of Ultra Shallow Junctions, (2008), p.75-94.

[2] M. P. Halsall et al., "Photomodulated Reflectivity Measurement of Free-Carrier Dynamics in InGaN/GaN Quantum Wells," ACS Photonics, vol. 5, no. 11, pp. 4437–4444, 2018, doi: 10.1021/acsphotonics.8b00904.

[3] F. Dortu, J. Bogdanowicz, T. Clarysse and W. Vandervorst, "Nonlinear study of photo electrothermal modulated optical reflectance for active dopant profile extraction," J. Appl. Phys., vol. 101, no. 5, 053107, 2007, doi: 10.1063/1.2464183.

[4] A. Pongrácz et al., "Tilt angle and dose rate monitoring of low energy ion implantation processes with photomodulated reflectance measurement: AM: Advanced Metrology," 2020 31st Annual SEMI Advanced Semiconductor Manufacturing Conference (ASMC), Saratoga Springs, NY, USA, 2020, pp. 1-4, doi: 10.1109/ASMC49169.2020.9185326.

[5] J. Szívós et al., "Monitoring of Dose Dependent Damage in MeV Energy Hydrogen Implanted Silicon by Photo-Modulated Reflectance Measurements," in IEEE Journal of the Electron Devices Society, vol. 10, pp. 761-768, 2022, doi: 10.1109/JEDS.2022.3178866.

[6] Aziz, M.J., Fundamentals of beam-solid interactions and transient thermal processing, (1988)

[7] C. W. White, J. Narayan, and R. T. Young, "Laser annealing of ion-implanted semiconductors," Science, vol. 204, no. 4392, pp. 461–468, May 1979, doi: 10.1126/science.204.4392.461.

[8] S. Earles et al., "Nonmelt Laser Annealing of 5-keV and 1-keV Boron-Implanted Silicon," IEEE Transactions on Electron Devices, vol. 49, no. 7, pp. 1118–1123, Jul. 2002, doi: 10.1109/TED.2002.1013265.

[9] A. Taiwo, Y. Son, J. Shin, and Y. A. Salawu, "Enhanced Activation in Phosphorous-Doped Silicon via Dual-Beam Laser Annealing," Materials, vol. 17, no. 17, p. 4316, 2024, doi: 10.3390/ma17174316

[10] J. Bogdanowicz, "Electrothermal theory of photomodulated optical reflectance on active doping profiles in silicon," J. Appl. Phys., vol. 108, no. 10, 104908, 2010, doi: 10.1063/1.3504652.

[11] J. Opsal, M. W. Taylor, W. L. Smith and A. Rosencwaig, "Temporal behavior of modulated optical reflectance in silicon," J. Appl. Phys., vol. 61, no. 1, pp. 240–248, 1987, doi: 10.1063/1.338863.

[12] J. Bogdanowicz et al., "Nondestructive extraction of junction depths of active doping profiles from photomodulated optical reflectance offset curves," J. Vac. Sci. Technol. B, 28(1), C1C1, 2010/2011. doi:10.1116/1.3271155

[13] Forget, B.C., Fournier, D. (1992). Surface Characterization by Modulated Photoreflectance. In: Bićanić, D. (eds) Photoacoustic and Photothermal Phenomena III. Springer Series in Optical Sciences, vol 69. Springer, Berlin, Heidelberg. https://doi.org/10.1007/978-3-540-47269-8_97

[14] James F. Ziegler, M.D. Ziegler, J.P. Biersack, SRIM – The stopping and range of ions in matter, Nuclear Instruments and Methods in Physics Research 1818-1823, ISSN 0168-583X, https://doi.org/10.1016/j.nimb.2010.02.091.

[15] S.M. Sze, Kwok K. Ng, Physics of Semiconductor Devices, doi.: 10.1002/0470068329, Wiley, 2007